Unsteady Flow Evolution and Combustion Dynamics of Homogeneous Solid Propellant in a Rocket Motor

SOURABH APTE and VIGOR YANG*

*Department of Mechanical and Nuclear Engineering, The Pennsylvania State University,
University Park, PA 16802, USA*

A time-resolved numerical analysis of combustion dynamics of double-base homogenous solid propellant in a rocket motor is performed by means of a Large-Eddy Simulation (LES) technique. The physiochemical processes occurring in the flame zone and their influence on the unsteady flow evolution in the chamber are investigated in depth. A five-step reduced reaction mechanism is used to obtain the two-stage flame structure consisting of a primary flame, a dark zone, and a secondary flame in the gas phase. It is observed that, for homogeneous solid propellant combustion, the chemical time scale is much greater than the smallest turbulence time scale, rendering a highly stretched and thickened flame. The chemical reactions proceed at a slower rate than turbulent mixing, and propellant combustion may be locally treated as a well-stirred reactor. The flowfield in the chamber consists of three regions of evolution: the upstream laminar regime, the central transitional section, and the fully developed turbulent regime further downstream. A theoretical formulation exploring the chamber flow and flame dynamics is established to study the intriguing phenomenon of combustion instability. The work done by Reynolds stresses, vorticity-flame interactions, and coupling between the velocity field and entropy fluctuations may cause resonance effects and excite pressure oscillations leading to self-sustained unsteady motions within the chamber.   © 2002 by The Combustion Institute

NOMENCLATURE

a = speed of sound
C_p = constant-pressure specific heat of gas
D_{ij} = binary mass diffusivity
D_{im} = effective molecular mass diffusivity of species i
E_i = activation energy
e = specific total energy
e_s = specific sensible energy
f = frequency
G = spatial filter
h_i = specific enthalpy of species i
h_s = total specific sensible enthalpy
I = turbulence intensity, $\sqrt{\overline{u'u'} + \overline{v'v'}}$
L = chamber length
$\dot{m}$ = mass flow rate
N = number of species in gas-phase reactions
Pr = Prandtl number
p = pressure
q = rate of heat release per unit volume
R = chamber radius
R_u = universal gas constant
Sc = Schmidt number
S_{ij} = strain-rate tensor, $\frac{1}{2}((\partial u_i/\partial x_j) + (\partial u_j/\partial x_i)) - \frac{1}{3} \delta_{ij}(\partial u_k/\partial x_k)$

St = Strouhal number
s = entropy
s_L = laminar flame speed
T = temperature
t = time
u, v = bulk velocities in axial and vertical directions, respectively
u_1, u_2 = bulk velocities in axial and vertical directions, respectively
$\hat{u}_1, \hat{u}_2$ = diffusion velocities in axial and vertical directions, respectively
$\mathbf{u}$ = velocity vector
v_w = radial injection velocity at propellant surface
V = specific volume
$\bar{W}_{mix}$ = molecular weight of mixture
W_i = molecular weight of species i
x, y = axial and radial coordinates, respectively
x_1, x_2 = axial and radial coordinates, respectively
Y_i = mass fraction of species i
Δ = filter width
δ_{ij} = Kronecker delta
η = length scale of small turbulent eddy
λ = thermal conductivity
ρ = density
σ = viscous stress
μ = dynamic viscosity

*Corresponding author. E-mail: vigor@psu.edu

ν = kinematic viscosity
$\dot{\omega}_i$ = rate of production of species i
Ω = vorticity

Subscripts

0 = head end
c = centerline
i = species i
p = propellant
s = sensible

Superscripts

a = periodic fluctuation
t = turbulent fluctuation
$'$ = sum of periodic and turbulent fluctuations
r = resolved scale
s = unresolved (subgrid) scale
$\tilde{}$ = density-weighted quantity
$\bar{}$ = time-averaged quantity

INTRODUCTION

This paper extends our previous work on combustion dynamics of double-base, homogeneous solid propellants in a rocket motor [1], to perform a comprehensive analysis of the results obtained from the Large-Eddy Simulation (LES). Emphasis is placed on the gas-phase physiochemical processes characterizing the microscale motions above the propellant surface and their effect on the macroscale motions in the bulk of the chamber. A theoretical formulation exploring the chamber flow and flame dynamics is developed to study the intriguing phenomenon of combustion instability. The response of the gas-phase flame to unsteady flow evolution in the chamber is addressed in depth.

Combustion instabilities in solid-propellant rocket motors have been explored extensively over the past few decades using analytical, experimental, and numerical techniques [2]. The dynamic coupling between propellant combustion and fluctuating chamber flow may lead to oscillations of heat-release distribution. The turbulence-enhanced heat and mass transfer rates modify the flame structure, which in turn affects the transient combustion response of

propellant. The amplitudes of these disturbances increase due to the resonance effect and are eventually limited by dissipation to render limit-cycle oscillations [3]. Many efforts have been made to analyze these driving mechanisms separately. Investigation of their collective effects in realistic rocket environments, however, has not been attempted.

Most of the earlier work in exploring the flow evolution in a rocket chamber was based on cold-flow studies with injection of inert gases through the sidewalls of the chamber simulating the gas influx from the burning propellant. In this idealized configuration, Taylor [4] and later Culick [5] obtained analytical expressions for the velocity distributions in laminar incompressible flows. The study was later extended by Balakrishnan et al. [6] to include the effects of rotationality and compressibility. Dunlap et al. [7] and Traineau et al. [8] conducted experiments for incompressible and compressible flows, respectively, to quantify the turbulence characteristics and mean velocity transitions in the chamber. Three regimes of flow evolution: the upstream laminar, transitional, and downstream turbulent regions, were identified. Beddini [9] and Sabnis et al. [10] applied turbulence closure models to obtain numerical results of the flowfield. The acoustic-wave excitation in solid rocket motors by vortex shedding was addressed by Flandro [11] and further investigated by Vuillot [12] in their cold-flow analyses. Recently, Apte and Yang [13, 14] performed time-resolved numerical simulations based on LES techniques to investigate the behavior of unsteady motor flowfields under conditions with and without externally imposed oscillations. The frequency spectra of flow oscillations obtained from these simulations were in qualitative agreement with the stability analysis performed by Casalis et al. [15] and Ugurtas et al. [16] for the parietal vortex-shedding in a channel with side-wall injection. Significant insight into the energy-transfer mechanisms among the mean, turbulent, and periodically oscillatory flowfields was obtained. The periodic oscillations give rise to energy exchange between the organized and turbulent motions, in addition to the well-established interactions between the mean and turbulent flowfields [14, 18]. This consequently produces enhanced turbulence in-

tensity and leads to earlier laminar-to-turbulence transition than that observed in stationary flows without acoustic forcing. The turbulence-enhanced momentum transport, on the other hand, promotes effective eddy viscosity and tends to dissipate the vortical wave generating from the injection surface. These LES-based cold-flow studies demonstrated their effectiveness in exploring unsteady motions in rocket chambers. It was also established that turbulence effects can best be modeled using LES for reacting flows to achieve the credibility of predictions from numerical simulations.

Although there have been several experimental and numerical studies on non-reacting flows in rocket motors, obtaining quantitative data for burning solid propellant under realistic conditions is a formidable challenge because of the complexities involved in the flowfield. For double-base homogeneous propellants, the flame standoff distance is around 1 mm at 25 atm. and decreases with increasing chamber pressure, leading to practical difficulties in obtaining accurate experimental data. The predictive capability of time-resolved numerical analysis is thus important to obtaining deep insight into the combustion phenomenon. In an effort to study the detailed coupling between propellant combustion dynamics and local flow oscillations in rocket motors, Yang and co-workers [19–22] conducted a series of numerical investigations into homogeneous propellant combustion under conditions representative of practical propulsion systems. Turbulence closure was achieved using a two-layer model calibrated for non-reacting motor flows. Much information has been obtained about the flame structure, heat-release mechanism, propellant combustion response, and flow development. Results indicate that the oscillatory flow characteristics were significantly altered because of the turbulence-enhanced mass and energy transport in the gas phase. As a consequence, the energy released in the flame zone and propellant combustion response were modified and caused significant changes in the motor stability behavior. Apte and Yang [1] recently extended the turbulence model adopted in those analyses by including a LES-based treatment. The intricate interactions among the acoustic, vortical, and entropy waves in a motor were examined.
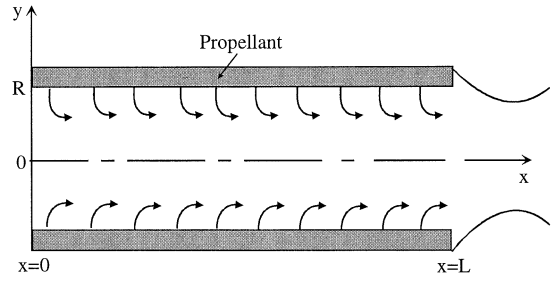

Fig. 1. Schematic diagram of a solid rocket motor.

The present work is a sequel to our previous study [1] and establishes a methodology to analyze the various mechanisms responsible for driving unsteady motions in a rocket motor. In subsequent sections, a theoretical formulation including chemical kinetics models and governing equations for time-resolved simulation of solid-propellant combustion in a cylindrical chamber is established. The interactions between turbulence and chemistry are then described in detail, followed by a brief summary of the numerical technique used in the analysis. Results obtained from the numerical simulation are presented. Finally, the self-sustained flow fluctuations within the chamber are analyzed, with special attention given to the effect of turbulence on the gas-phase flame dynamics.
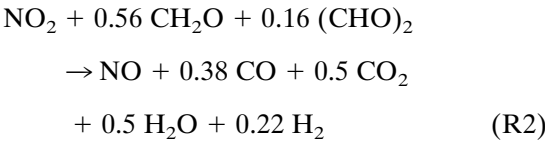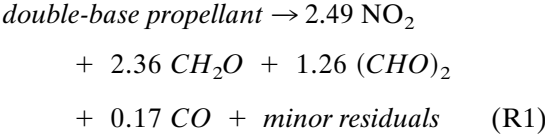
THEORETICAL FORMULATION

Figure 1 shows a schematic diagram of the cylindrical combustion chamber analyzed herein, which is loaded with a double-base propellant grain along the entire azimuth and connected downstream to a choked convergent-divergent nozzle. The propellant undergoes degradation in a thin superficial layer underneath the burning surface. The pyrolysis products are injected into the combustion chamber and react to form a multistage flame in the gas phase [20].
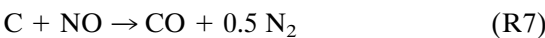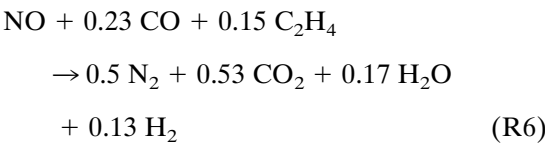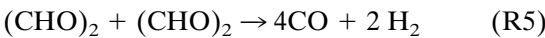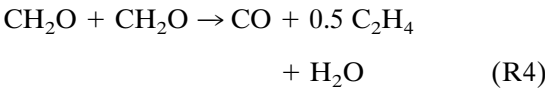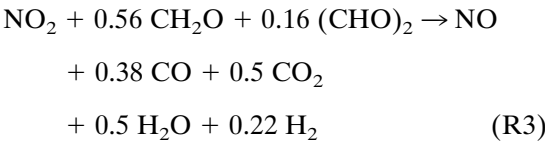
Chemical Kinetics Model

Owing to the difficulties in establishing a complete chemical kinetics scheme and limitations of computational resources, a thorough consideration of all physical and chemical processes does not appear feasible. A reduced reaction mecha-

nism is therefore used to describe the combustion wave structure in both the gas and condensed phases [20]. The scheme has been well established and provides reasonably accurate information about the major chemical kinetic pathways. The chemical behavior of the condensed phase is described by two reactions: solid propellant decomposition (R1) and reaction of NO_2 (R2), providing elementary species such as NO_2, NO, and aldehydes to maintain the gas-phase flames.

$$double\text{-}base\ propellant \rightarrow 2.49\ NO_2$$

$$+\ 2.36\ CH_2O\ +\ 1.26\ (CHO)_2$$

$$+\ 0.17\ CO\ +\ minor\ residuals \quad \text{(R1)}$$

$$NO_2 + 0.56\ CH_2O + 0.16\ (CHO)_2$$

$$\rightarrow NO + 0.38\ CO + 0.5\ CO_2$$

$$+\ 0.5\ H_2O + 0.22\ H_2 \quad \text{(R2)}$$

The stoichiometric coefficients in reaction (R1) are determined based on the composition of a "hot" double-base propellant containing 52% nitrocellulose (NC), 43% nitroglycerin (NG), and 5% minor additives. The heat of combustion of the propellant is about 1100 cal/g.

The gas-phase chemical kinetics is specified by five reactions: two first-order NO_2 and NO-carbon reactions, and three second-order reactions involving aldehydes and NO. These reactions represent the most important and slowest steps limiting the reaction rates in the gas phase:

$$NO_2 + 0.56\ CH_2O + 0.16\ (CHO)_2 \rightarrow NO$$

$$+\ 0.38\ CO + 0.5\ CO_2$$

$$+\ 0.5\ H_2O + 0.22\ H_2 \quad \text{(R3)}$$

$$CH_2O + CH_2O \rightarrow CO + 0.5\ C_2H_4$$

$$+\ H_2O \quad \text{(R4)}$$

$$(CHO)_2 + (CHO)_2 \rightarrow 4CO + 2\ H_2 \quad \text{(R5)}$$

$$NO + 0.23\ CO + 0.15\ C_2H_4$$

$$\rightarrow 0.5\ N_2 + 0.53\ CO_2 + 0.17\ H_2O$$

$$+\ 0.13\ H_2 \quad \text{(R6)}$$

$$C + NO \rightarrow CO + 0.5\ N_2 \quad \text{(R7)}$$

The rates of production of each constituent species in the gas and condensed phases and the physiochemical properties are given in Refs. 17 and 20. In the present work, emphasis is placed on the gas-phase combustion dynamics to explore the physiochemical processes occurring near the propellant surface and their overall effect on the complex flow physics within the chamber. A detailed numerical analysis involving the dynamic coupling between the condensed and gas phases has been studied for both laminar and turbulence flows using second-order turbulence closure models [21, 22], and can be extended further to perform LES-based computations.

Gas-Phase Governing Equations

The five-step combustion model described above is important to predict the two-stage flame structure accurately. The finite-rate chemical kinetics and steep gradients near the burning surface, on the other hand, require small time-steps for numerical stability. Because of the intricacy of the problem, which involves a wide range of length and time scales, and the limitations of computational resources, the analysis deals only with the conservation laws in axisymmetric coordinates. This treatment lacks the vortex-stretching phenomenon commonly observed in turbulent flows and may under-predict the turbulence production and dissipation rates. The model, nonetheless, allows for a systematic investigation into the interactions between propellant combustion and motor flow development. Much useful information can be obtained about the effect of turbulence on flame dynamics, especially in the near-surface region. A recent study of rocket motor internal flow based on a comprehensive three-dimensional, LES technique [17, 23] indicates that the two-dimensional simulation indeed can capture the salient features of turbulent flows and leads to good agreement with experimental data in terms of mean flow properties and acoustic-wave induced flow oscillations.

A spatial filter G is employed to decompose the flow variables into a large (resolved) and a subgrid (unresolved) scale

$$\Im(\mathbf{x}, t) = \Im^r(\mathbf{x}, t) + \Im^s(\mathbf{x}, t)$$

$$\text{with} \quad \Im^r(\mathbf{x}, t)$$

$$= \int_D G(\mathbf{x} - \mathbf{x}', \Delta)\Im(\mathbf{x}', t)\ d^3x' \quad \text{(1)}$$

where D is the entire domain, Δ the filter size which determines the size of the unresolved scale, and $\Im$ any flow property: ρ, u, v, T, or Y_i. The superscripts r and s represent the resolved and unresolved scales of flow properties, respectively. Favre averaging is further used to simplify the governing equations for compressible turbulent-flow simulation.

$$\tilde{\Im}^r = \frac{(\rho\Im)^r}{\rho^r} \tag{2}$$

The filtered conservation equations for axisymmetric configuration can be written as

mass

$$\frac{\partial(x_2\rho^r)}{\partial t} + \frac{\partial(x_2\rho^r\tilde{u}_k^r)}{\partial x_k} = 0 \tag{3}$$

axial momentum

$$\frac{\partial(x_2\rho^r\tilde{u}_1^r)}{\partial t} + \frac{\partial(x_2\rho^r\tilde{u}_1^r\tilde{u}_1^r)}{\partial x_1} + \frac{\partial(x_2\rho^r\tilde{u}_1^r\tilde{u}_2^r)}{\partial x_2} = -\frac{\partial(x_2 p^r)}{\partial x_1} + \frac{\partial(x_2\sigma_{11}^r)}{\partial x_1} + \frac{\partial(x_2\sigma_{12}^r)}{\partial x_2} + \frac{\partial(x_2\tau_{u_1u_1})}{\partial x_1}$$

$$+ \frac{\partial(x_2\tau_{u_1u_2})}{\partial x_2} - \left\{ \frac{2}{3}\frac{\partial}{\partial x_1}(\mu u_2)^r \right\} \tag{4}$$

radial momentum

$$\frac{\partial(x_2\rho^r\tilde{u}_2^r)}{\partial t} + \frac{\partial(x_2\rho^r\tilde{u}_2^r\tilde{u}_1^r)}{\partial x_1} + \frac{\partial(x_2\rho^r\tilde{u}_2^r\tilde{u}_2^r)}{\partial x_2} = -\frac{\partial(x_2 p^r)}{\partial x_2} + \frac{\partial(x_2\sigma_{21}^r)}{\partial x_1} + \frac{\partial(x_2\sigma_{22}^r)}{\partial x_2} + \frac{\partial(x_2\tau_{u_2u_1})}{\partial x_1}$$

$$+ \frac{\partial(x_2\tau_{u_2u_2})}{\partial x_2} - \left\{ p^r - \frac{4}{3}\left(\mu\frac{u_2}{x_2}\right)^r + \frac{2}{3}\left(\mu\frac{\partial u_1}{\partial x_1}\right)^r \right.$$

$$\left. - \frac{2}{3}\left(u_2\frac{\partial\mu}{\partial x_2}\right)^r \right\} \tag{5}$$

energy

$$\frac{\partial(x_2\rho^r\tilde{e}_s^r)}{\partial t} + \frac{\partial(x_2\rho^r\tilde{h}_s^r\tilde{u}_k^r)}{\partial x_k} = -\frac{\partial(x_2 q_k^r)}{\partial x_k} - \frac{\partial(x_2\tau_{u_kh})}{\partial x_k} - \frac{\partial(x_2\tau_{u_ku_lu_l})}{\partial x_k} + \frac{\partial(x_2 u_l\sigma_{kl})^r}{\partial x_k} - \sum_{i=1}^{N} h_{f_i}^0\dot{\omega}_i^r$$

$$+ \left\{ -\frac{2}{3}\frac{\partial}{\partial x_1}(\mu u_1 u_2)^r - \frac{2}{3}\frac{\partial}{\partial x_2}(\mu u_2^2)^r \right\} \tag{6}$$

species concentration

$$\frac{\partial(x_2\rho^r\tilde{Y}_i^r)}{\partial t} + \frac{\partial(x_2\rho^r\tilde{Y}_i^r\tilde{u}_k^r)}{\partial x_k} = -\frac{\partial(x_2 q_{i_k}^r)}{\partial x_k}$$

$$- \frac{\partial(x_2\tau_{u_kY_i})}{\partial x_k} + \dot{\omega}_i^r \tag{7}$$

where the terms in curly brackets represent the resolved part of the axisymmetric source terms. For a multi-component mixture, the pressure p^r, specific sensible internal energy $\tilde{e}_s^r$, and specific sensible enthalpy $\tilde{h}_s^r$ follow the definitions given below

$$p^r = \rho^r R_u \tilde{T}^r \sum_{i=1}^{N} \frac{\tilde{Y}_i^r}{W_i}$$

$$\tilde{e}_s^r = \sum_{i=1}^{N} \int_{T_{ref}}^{T} \tilde{Y}_i^r C_{pi}\, dT - \frac{p^r}{\rho^r} + \frac{\tilde{u}_1^{r2} + \tilde{u}_2^{r2}}{2} \tag{8}$$

$$\tilde{h}_s^r = \sum_{i=1}^{N} \int_{T_{ref}}^{T} \tilde{Y}_i^r C_{pi}\, dT + \frac{\tilde{u}_1^{r2} + \tilde{u}_2^{r2}}{2}$$

Note that instead of using the conventional "total energy" formulation, the energy equation is written with heat of reaction $(-\Sigma_{i=1}^{N} h_{f_i}^0\dot{\omega}_i^r)$ as

a source term, for which accurate experimental data is available [20].

The shear and normal stresses are given by

$$\sigma_{kl}^r = \mu\left(\frac{\partial \bar{u}_k^r}{\partial x_l} + \frac{\partial \bar{u}_l^r}{\partial x_k} - \frac{2}{3}\left(\frac{\partial \bar{u}_i^r}{\partial x_i} + \frac{\bar{u}_2^r}{x_2}\delta_{kl}\right)\right) \quad (9)$$

The diffusion term q_k^r consists of contributions from heat conduction and mass diffusion processes.

$$q_k^r = -\lambda\frac{\partial \tilde{T}^r}{\partial x_k} + \rho^r\sum_{i=1}^N (\hat{h}_i\tilde{Y}_i\hat{u}_k)^r \quad (10)$$

The species diffusion term $q_{i_k}^r$ is calculated using Fick's law

$$q_{i_k}^r = \rho^r\tilde{Y}_i\hat{u}_k = -\rho^r D_{im}\frac{\partial \tilde{Y}_i^r}{\partial x_k} \quad (11)$$

where D_{im} is the effective molecular mass-diffusion coefficient for species i.

The terms $\tau_{u_k u_l}$, $\tau_{u_k h}$, and $\tau_{u_k Y_m}$ are the sub-grid scale (sgs) stresses, heat fluxes, and species mass fluxes, respectively. These terms, along with the triple correlation $\tau_{u_k u_l u_l}$, the viscous dissipation rate $(u_l\sigma_{kl})^r$ and the filtered chemical source terms, require closure models. A Smagorinsky model extended to reacting flows is used to compute these terms [24]. The sgs-stresses are given as

$$\tau_{u_k u_l} = -\rho^r((u_k u_l)^r - \bar{u}_k^r\bar{u}_l^r)$$

$$= 2C_R\rho^r\Delta^2\Pi_{\tilde{S}}^{1/2}\left(\tilde{S}_{kl}^r - \frac{1}{3}\tilde{S}_{ii}^r\delta_{kl}\right)$$

$$- \frac{2}{3}C_I\rho^r\Delta^2\Pi_{\tilde{S}}\delta_{kl} \quad (12)$$

where Δ is the average size of the computational cell. $C_R(\approx 0.01)$ and $C_I(\approx 0.007)$ are the model constants based on Erlebacher et al. [25]. The quantities $\Pi_{\tilde{S}}$, $\tilde{S}_{kl}^r$ are defined, respectively, as

$$\Pi_{\tilde{S}} = \tilde{S}_{kl}^r\tilde{S}_{kl}^r \quad (13)$$

$$\tilde{S}_{kl}^r = \frac{1}{2}\left(\frac{\partial \bar{u}_k^r}{\partial x_l} + \frac{\partial \bar{u}_l^r}{\partial x_k}\right) - \frac{1}{3}\delta_{kl}\left(\frac{\partial \bar{u}_i^r}{\partial x_i}\right) \quad (14)$$

The sgs heat and species mass fluxes are similarly obtained as

$$\tau_{u_k h} = -\rho^r C_p\frac{C_R}{Pr_T}\Delta^2\Pi_{\tilde{S}}^{1/2}\frac{\partial \tilde{T}^r}{\partial x_k} \quad (15)$$

$$\tau_{u_k Y_i} = -\rho^r\frac{C_R}{Sc_T}\Delta^2\Pi_{\tilde{S}}^{1/2}\frac{\partial \tilde{Y}_i^r}{\partial x_k} \quad (16)$$

The turbulent Prandtl and Schmidt numbers (Pr_T and Sc_T) are assigned a value of 0.4 [25]. The triple correlation $\tau_{u_k u_l u_l}$ accounts for the interactions between the resolved velocity vector and the sgs kinetic energy, and is modeled as follows [26]:

$$\tau_{u_k u_l u_l} = -\bar{u}_l^r\left(2C_R\rho^r\Delta^2\Pi_{\tilde{S}}^{1/2}\left(\tilde{S}_{kl}^r - \frac{1}{3}\tilde{S}_{ii}^r\delta_{kl}\right)\right) \quad (17)$$

Turbulence/Flame-Structure Interaction

The reaction rates $\dot{\omega}_i$ in the species-concentration equations need to be modeled to capture the effect of subgrid scales on chemical reactions. Peters [27, 28] examined the problem of turbulence/chemistry interactions for premixed flames in terms of three non-dimensional parameters: turbulent Reynolds number Re_t, turbulent Damkohler number Da, and turbulent Karlovitz number Ka, as defined below

$$\mathrm{Re}_t \sim \frac{v'}{s_L}\frac{\ell_t}{\ell_F} \quad (18)$$

$$Da = \frac{t_t}{t_F} \sim \frac{\ell_t/v'}{\ell_F/s_L} \quad (19)$$

$$Ka = \frac{t_F}{t_K} \sim \left(\frac{v'}{s_L}\right)^{3/2}\left(\frac{\ell_t}{\ell_F}\right)^{-1/2} \quad (20)$$

where t_t, t_F, and t_K represent the turbulent-eddy, characteristic flame, and Kolmogorov time scales, respectively. The turbulent Damkohler and Karlovitz numbers are expressed in terms of laminar flame thickness ℓ_F, flame speed $s_L \sim v_w$, turbulent length scale ℓ_t, and turbulence intensity v'. Figure 2 (taken from Peters [27, 28]), commonly referred to as the regime diagram for premixed turbulent combustion, shows the variation of v'/s_L with ℓ_t/ℓ_F. The Damkohler number on this log-log plot corresponds to the inverse slope of a line as can be seen from Eq. 19. Also shown are two constant Karlovitz-number lines, $Ka = 1$ and 100, where $Ka_\delta = 100\ Ka$ corresponds to the Karlovitz number based on the inner reaction
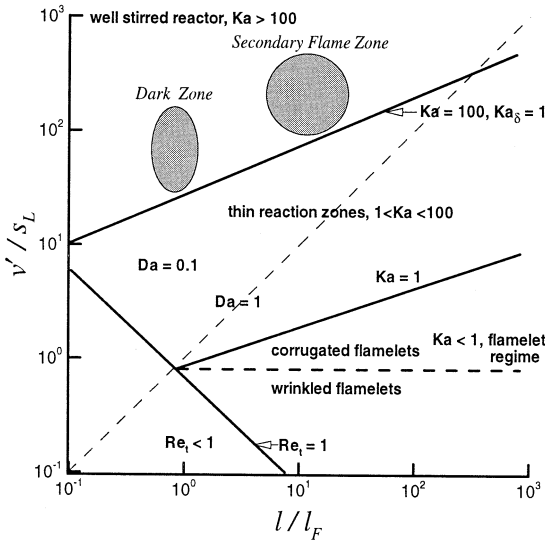
Fig. 2. Phase diagram showing different regimes in pre-mixed turbulent combustion.

layer, $\ell_\delta = \delta\ell_F$. Peters [28] argues that for premixed flame structures there exist a chemically inert preheat zone with thickness of the order of the flame thickness and a thin reaction layer (called inner layer) where the majority of the heat release occurs. The inner layer is followed by a post-flame oxidation layer where the final products are formed. For hydrocarbon premixed flames, $\delta \sim 0.1$ typically and the thin inner layer controls the overall flame structure.

Four different regimes in premixed turbulent combustion are identified based on the relative magnitudes of these parameters, as illustrated in Fig. 2. If chemical reactions proceed at rates lower than those of turbulent mixing (i.e., $Da < 1$), and the flame stretch is strong enough to cause penetration of small eddies into the flame zone (i.e., $Ka > 1$), then the chemical kinetics become sufficiently slow to result in thick flames. For $Re_t > 1$, $Ka > 1$, and $Ka < 100$, the inner reaction layer is thin, $\ell_F > \eta > \ell_\delta$. In this situation, the small eddies which cannot penetrate into the reaction zone can enter the preheat zone to increase scalar mixing and consequently destroy the quasi-steady flamelet structure that exists in the corrugated flamelet regime ($Ka < 1$). The flamelet theory can still be applied to this regime and agrees well with the flamelet boundary obtained in numerical studies of Poinsot et al. [29], where two-dimen-

sional interactions between a laminar premixed flame front and a vortex pair were analyzed. For $Ka > 100$, the flames become thick and $\ell_F > \ell_\delta > \eta$. Small eddies can now penetrate into the reaction zone, and modify the flame structure. For $Ka > 100$ and $Da < 1$, turbulence is weak and no direct interactions between turbulence and combustion occur in this regime. The flame structure can be locally modeled as a well-stirred reactor. Turbulence, however, modifies the mixing rate through eddy viscosity and diffusivity.

In Fig. 2, the Da and Ka numbers are estimated for different regimes of the two-stage flame structure of homogeneous solid propellant combustion. Accordingly, estimates of the laminar and turbulent velocity scales are obtained in the turbulent regime for the present simulation conditions (described later). For the head-end pressure of 2.5 MPa, the propellant regression rate and density are $r_b = 4.8$ mm/s and $\rho_p = 1620$ kg/m^3, respectively. From the mass balance across the interface between the condensed and gaseous phases ($\rho_p r_b = \rho_g v_w$), the gas-phase injection velocity (v_w) can be obtained. This injection velocity is in fact the laminar flame speed (s_L). Typically, for $\rho_g \approx 12.2$ kg/m^3, the flame speed is ~ 0.8 m/s. As shown later in the paper, the secondary flame thickness and peak turbulence intensity in the fully turbulent regime are approximately 1 mm and 70 m/s, respectively. Based on these estimates, typical Karlovitz (Ka) and Damkohler (Da) numbers are in the range of 100–200, 0.2–0.4, respectively. These are represented in the premixed-flame phase diagram. Tseng and Yang [19] also corroborated that for double-base homogeneous propellants, Ka is large and $Da < 1$. They "locally" modeled the turbulence/flame-structure interactions as well-stirred.

As shown later in the present study, the turbulent Reynolds, Damkohler, and Karlovitz numbers vary in the axial direction. Their radial distributions in the turbulent flame region, however, fall in the regime of $Da < 1$ and $Ka > 100$. Under these conditions, turbulence rapidly penetrates into the flame zone through enhanced mass transfer, leaving chemical reactions as the rate-controlling processes. Accordingly, the closure for reaction rates follows the standard approximation of resolved reaction rates [17, 24]

$$\dot{\omega}_i^r = \dot{\omega}_i^r(\rho, T, Y_1, Y_2, \ldots, Y_N)$$

$$= \dot{\omega}_i(\rho^r, \bar{T}^r, \bar{Y}_1^r, \bar{Y}_2^r, \ldots, \bar{Y}_N^r) \qquad (21)$$

The above model allows for fluctuations in the rates of species production as functions of instantaneous flow properties, and thus is less stringent than that used in the second-order turbulence-closure scheme [19].

Boundary Conditions

The present work focuses on gas-phase flame dynamics, with the propellant surface conditions specified based on their values at the chamber head-end. The surface properties are first obtained by solving the coupled species-concentration equations in the gas and condensed phases, with proper interfacial boundary conditions conserving mass and energy at the head-end of the chamber [17, 20]. Results of flame structure and temperature agree well with experimental data over a wide range of pressure. The burning rate, surface temperature, and species concentrations remain fixed throughout the entire motor accordingly. Following the method of characteristics, the exit plane requires no physical boundary condition, since the flow is supersonic downstream of the nozzle throat. At the upstream boundary, the axial velocity and pressure gradient, as well as the radial velocity gradient, are set to zero along the solid wall. The last condition is required to prevent the occurrence of a numerically produced recirculating flow at the head end [19]. The mass burning rate, total temperature, and species mass fluxes are fixed at the propellant surface. Normal injection of the pyrolysis products is enforced by employing the no-slip boundary condition. Finally, flow symmetry is assumed at the centerline. In order to perturb the flowfield to obtain transition to turbulence, pseudo-turbulence in the form of white noise is introduced at the propellant surface, with spatial and temporal fluctuations in the mass-flow rate within 1% of the mean value.

NUMERICAL METHOD

One characteristic trait of solid-propellant rocket motor internal flowfields is that the Mach number varies from zero at the head end to unity at the nozzle throat as the flow accelerates rapidly in the downstream region. In the low-Mach number region, the inviscid compressible form of the conservation equations is poorly coupled and stiff [30]. The associated disparity among the eigenvalues results in significant slowdown in convergence. Chemical reactions exhibit another category of numerical difficulties because of the wide ranges of time and length scales involved. In regions where reaction rates are high, species mass concentrations may vary rapidly over a short period of time, and numerical stability may require an enormous number of iterations. To avoid this stiffness problem, chemical source terms are usually treated implicitly, in a method analogous to preconditioning the time derivative terms of the species conservation equations so that all chemical and convective processes proceed at approximately the same numerical rate.

In the present work, a preconditioning technique along with the dual-time stepping integration procedure described in Refs. 17 and 30 is first used to establish a stable flame and eliminate the initial transients in the flowfield. A time-accurate, semi-implicit Runge-Kutta scheme with fourth-order central differencing for spatial discretization is then employed because the preconditioning method is computationally expensive and difficult to parallelize. A detailed description of the numerical scheme and parallel implementation is provided in Ref. 17.

RESULTS AND DISCUSSION

Figure 1 shows the subject physical model, consisting of an axisymmetric rocket motor connected downstream to a choked nozzle. The chamber measures 55 cm in length and 2 cm in diameter, and is loaded with a double-base homogeneous solid propellant grain (53% NC and 42% NG and minor additives) over the entire azimuth. The high aspect ratio chosen here ensures occurrence of turbulence in the downstream region. The nozzle throat area is set based on a contraction ratio of 1.25, which leads to high Mach numbers and low pressures in the downstream region. The head-end pres-

sure is around 2.5 MPa. Although it is lower than the usual operating range for solid propellant rocket motors, it serves two purposes. First, the lower gas-phase density renders a higher injection velocity and a shorter chamber for transition to turbulence in the downstream. Second, the higher injection rate increases the flame standoff distance and thus reduces the degree of grid-stretching required to resolve the primary flame. The mass flux at the propellant surface is 8.1 kg/m^{2}s, and the corresponding injection Reynolds and Mach numbers are 10^4 and 1.85×10^3, respectively. The surface temperature is fixed at 640 K.

The steep temperature gradient near the propellant surface in the gas and condensed phases dictates the numerical grid resolution required to accurately capture the combustion wave structure. A detailed grid dependence study was performed to obtain the optimal grid spacing in the radial direction near the surface. To predict the burning surface conditions by solving the coupled gas- and condensed-phase conservation equations with appropriate interfacial conditions, the smallest grid spacing on the order of 1 μm is necessary at the propellant surface [20–22]. This allows accurate computation of the steep temperature gradient at the surface and provides correct heat feedback to the condensed phase to determine the burning surface properties. In the present study, however, we focus on the gas-phase flame dynamics, and the condensed-phase effects appear through specified surface parameters as boundary conditions. A coarser grid is found to be sufficient to obtain the correct behavior of the flame structure [17]. Accordingly, 650×150 grids are used in the axial and radial directions, respectively. The smallest grid spacing normal to the surface is about 10 μm. Good resolution in the axial direction is necessary to resolve the turbulence kinetic-energy spectrum correctly. A time-step of 50 nanoseconds is employed to achieve numerical stability and accurate temporal resolution of the flame dynamics. Statistically meaningful turbulence properties are acquired by time-averaging numerical results over a span of 15 ms (about 3–4 flow-through times) after obtaining a stationary solution for the flame structure.

Vortical Dynamics

Figure 3 shows the time evolution of the azimuthal vorticity field in the combustion chamber. Only the lower half of the chamber is presented to facilitate discussion, where y/R = 1 corresponds to the burning surface. Vorticity is produced at the propellant surface because of the no-slip condition [11]. At the injection surface, $\Omega_z = (\partial \bar{v}^r / \partial x - \partial \bar{u}^r / \partial y)_w$. As the flow accelerates in the axial direction, pressure and density decrease while the injection velocity (v_w) increases to keep the mass flow rate ($\dot{m}_w$) constant. The axial variation of v_w, however, is not significant and the vorticity is mainly dictated by the radial gradient of the axial velocity. Near the head-end, the fluctuations in vorticity appear to be small and the flow is mostly laminar. Transition to turbulence occurs around $x/R = 25$ and the flow becomes highly turbulent further downstream. The magnitude of vorticity at the burning surface increases non-linearly along the axial direction and the size of the vortical structures grows in the downstream. The upstream vortical disturbance originating close to the wall overtakes a neighboring downstream disturbance since it is convected at a higher speed. As these vortical structures travel away from the wall, their size grows and results in large-scale mixing in the downstream.

The evolution of vorticity is governed by the Crocco-Vazsonyi equation which can be derived by taking the curl of the momentum equation.

$$\frac{D\mathbf{\Omega}}{Dt} = (\mathbf{\Omega} \cdot \nabla)\mathbf{u} - \mathbf{\Omega}(\nabla \cdot \mathbf{u}) - \nabla V \times \nabla p$$

$$+ \nu \nabla^2 \mathbf{\Omega} - \mu \nabla V \times (\nabla \times \mathbf{\Omega}) + \frac{4}{3}\mu \nabla V$$

$$\times \nabla(\nabla \cdot \mathbf{u}) \qquad (22)$$

where $\mathbf{\Omega}$ is the vorticity vector defined as $\nabla \times \mathbf{u}$, and $V = 1/\rho$ the specific volume. In an axisymmetric flow without heat release and viscous effects, the vorticity of a given fluid particle is conserved. In the present case, the conservation property of vorticity is no longer valid because of viscous dissipation, $-\mu\nabla(V) \times (\nabla \times \mathbf{\Omega}) + \frac{4}{3}\mu\nabla(V) \times \nabla(\nabla \cdot \mathbf{u})$, volume dilatation, $-\mathbf{\Omega}(\nabla \cdot \mathbf{u})$, and baroclinicity, $-\nabla V \times \nabla p$, resulting from the misalignment between the den-
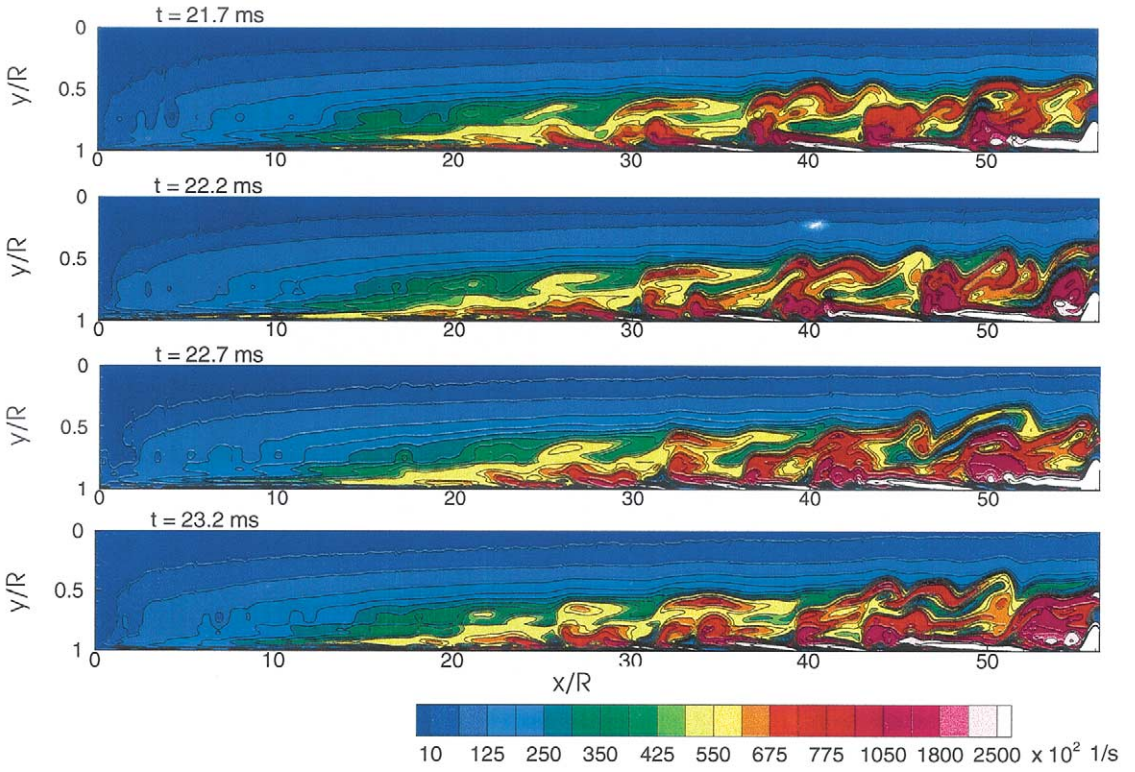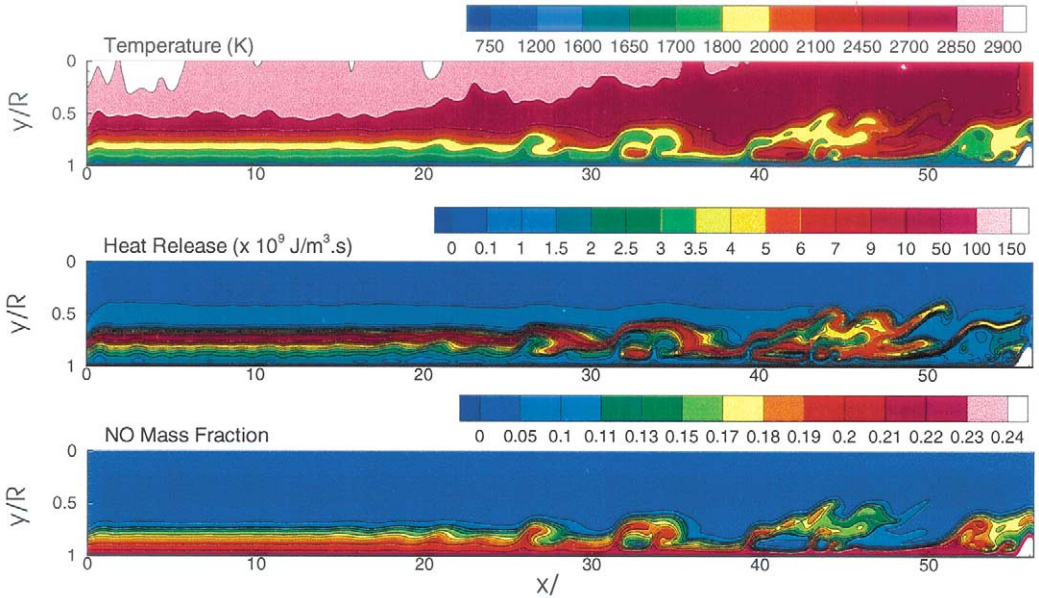
Fig. 3. Time evolution of vorticity field.

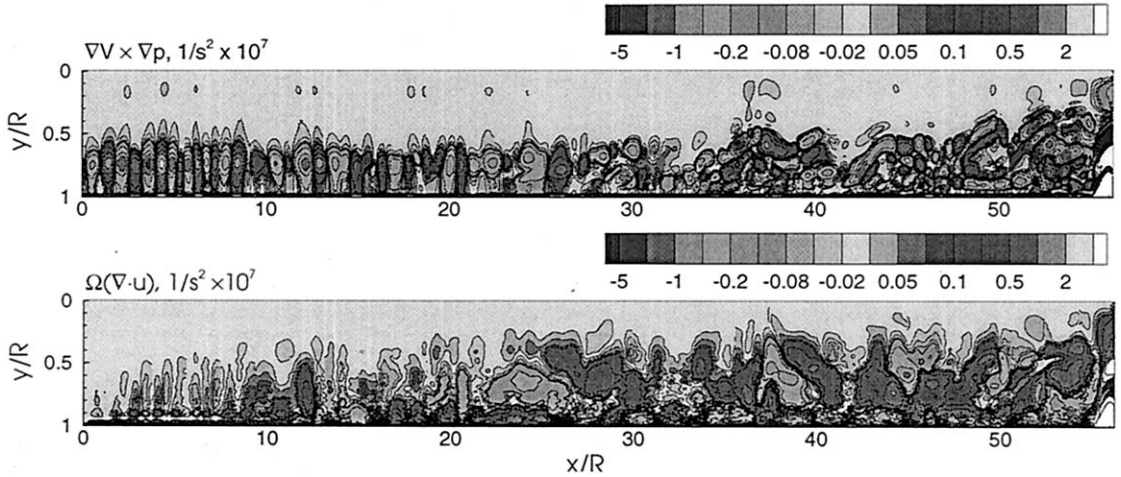Fig. 6. Snapshots of temperature, heat-release, and NO mass-fraction fields, t = 21.7 ms.

Fig. 4. Effects of baroclinicity and volume dilatation on evolution of vortical flowfield, t = 21.7 ms.

sity and pressure gradients. Vorticity created at the propellant surface is convected by the mean flow and is transported by viscous diffusion $(\nu \nabla^2 \mathbf{\Omega})$.

Figure 4 shows the snapshots of the baroclinic and dilatation effects that modify the vorticity transport within the chamber. In the flame zone, density varies dramatically so that volume dilatation and baroclinicity become predominant and viscous dissipation gives negligible contribution to the vorticity evolution. The decrease in density across the flame zone implies that the volume dilatation, $-\mathbf{\Omega}(\nabla \cdot \mathbf{u})$, acts as a sink term in Eq. 22, decreasing the vorticity level in the flame zone. Similarly, the baroclinic effect attempts to diminish the vorticity in the flame zone. The present axisymmetric computation lacks the vortex-stretching mechanism, $(\mathbf{\Omega} \cdot \nabla)\mathbf{u}$, responsible for transfer of energy from the large to the small scales through the energy cascade process, and leads to lower dissipation and production rates. Nevertheless, it provides much useful insight into the flow development and its interactions with the propellant flame dynamics, which was lacking in previous numerical studies using second-order turbulence closure schemes.

Figure 5 shows the power density spectra of axial velocity fluctuations (u'), normalized with the maximum centerline velocity at the chamber exit ($\bar{u}_r$), at two radial locations in the fully turbulent regime, x/R = 40. Here, the fluctuating variable is obtained by subtracting the time-mean value from its instantaneous quantity. The

peak magnitude of u' increases as the flow accelerates in the axial direction [17]. The distinct peaks at frequencies of 2.2, 3.1, and 6.1 kHz may correspond to the combined effects of hydrodynamic instability causing vortex-shedding and acoustic resonance within the motor. The halving of the dominant frequency away from the surface is indicative of the vortex-pairing mechanism commonly observed in turbulent shear flows. The same phenomenon was found by Dunlap et al. [7] in their cold-flow experiments in a porous chamber with surface mass injection simulating propellant burning. Recently, Casalis et al. [15] and Ugurtas et al.
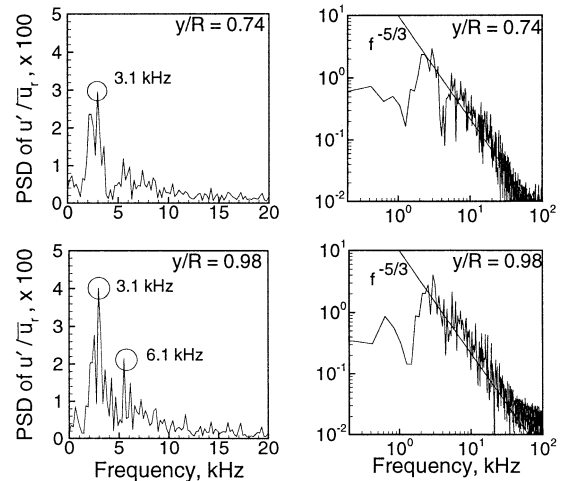

Fig. 5. Power density spectra of axial velocity fluctuations at two radial locations, x/R = 40.

[16] conducted linear stability analyses and experimental measurements of non-reacting injection-driven flows in porous chambers. The power density spectra obtained from cold-flow simulations by Apte and Yang [13, 23] were in qualitative agreement with these theoretical predictions. The Strouhal number, defined as $St = fR/v_w$ to characterize the parietal vortex shedding in the chamber, was found to be around 6 for pure hydrodynamic instabilities without acoustic resonance. For the present reacting-flow simulation, however, the Strouhal number is around 10 and varies significantly within the combustion chamber because of steep density and temperature gradients in the flame zone. The deviation in the Strouhal number may be attributed to the flame-vortex interactions modifying the vorticity evolution in the flame regime. The local Reynolds number is changed significantly by the presence of the flame, which alters the hydrodynamic instability characteristics. The ability of LES to predict such unsteady flowfields must be explored further in order to reveal important combustion instability phenomena in rocket chambers. The energy spectra are also shown on a log-log scale and compared with the Kolmogorov-Obukhov spectrum (i.e., the $-5/3$ law) obtained for homogeneous turbulence at large Reynolds numbers. The cut-off frequency of the present calculation lies in the inertial subrange of the turbulent energy spectrum, further ensuring that the large-scale motions are correctly resolved.

Flame Dynamics

The temporal evolution of the temperature field and associated heat-release distribution gives direct insight into the turbulent combustion mechanism. The instantaneous heat-release is given by the source term $(-\Sigma_{i=1}^{N} h_{f_i}^0 \dot{\omega}_i^r)$ in the energy equation. Figure 6 shows snapshots of the temperature, heat-release, and NO mass-fraction fields. In the laminar regime, the temperature increases rapidly within 0.25 mm from 640 K at the surface to around 1600 K at the end of the primary flame, which is followed by a dark zone of thickness 1.2 mm. The temperature further rises to its final value of 2850 K downstream of the secondary flame. The flame

fluctuates significantly in the turbulent regime owing to the vigorous vortical motions and the dark-zone thickness is substantially reduced. The intensive heat-release contours indicate a fluctuating flame front corresponding to the secondary flame zone, whose thickness is of the order of 1 mm. The highly exothermic reduction of NO to N_2 (R6) provides the major heat source in the secondary flame zone. NO is first formed near the surface through the reaction of NO_2 and aldehydes (R2 and R3). Turbulence-enhanced mixing results in rapid depletion of NO in the dark zone because of increased local temperature and the release of a large amount of energy. NO and CO then react in the secondary flame zone to give the final products.

To explore the microscale motions above the propellant surface, a close-up view of the flame structure and vorticity contours is shown in Fig. 7. For the present flow conditions, the temperature gradient at the burning surface remains unaffected even in the turbulent regime. Small-scale fluctuations in vorticity, temperature, heat-release, and NO mass-fraction near the surface indicate that turbulence does not penetrate significantly to modify the primary flame structure. For higher Reynolds numbers, however, turbulence may penetrate into the primary flame structure and consequently alter the propellant combustion response, a phenomenon commonly referred to as erosive burning [19].

In the present analysis of homogeneous-propellant combustion dynamics, the reaction-zone thickness was shown to be larger than the Kolmogorov length scale and turbulent combustion can be locally modeled as a well-stirred reactor (see Fig. 2). To further verify this treatment, radial distributions of the turbulent Reynolds, Karlovitz, and Damkohler numbers were obtained from the present simulations. It should be, however, noted that Re_t, Ka, and Da numbers were related to the flow, chemical and turbulent time scales. The chemical time and length scales may differ from the flame-characteristic scales, and thus Re_t, Ka, and Da are obtained locally from $Re_t = k^2/\nu\epsilon$, $Da = (k/\epsilon)/(\dot{\omega}_i/\rho)$, and $Ka = (\dot{\omega}_i/\rho)\sqrt{\epsilon/\nu}$, where k and ϵ represent the turbulent kinetic energy and its dissipation rate, respectively. These are obtained locally from numerical computations and are shown in Fig. 8 for a typical location of
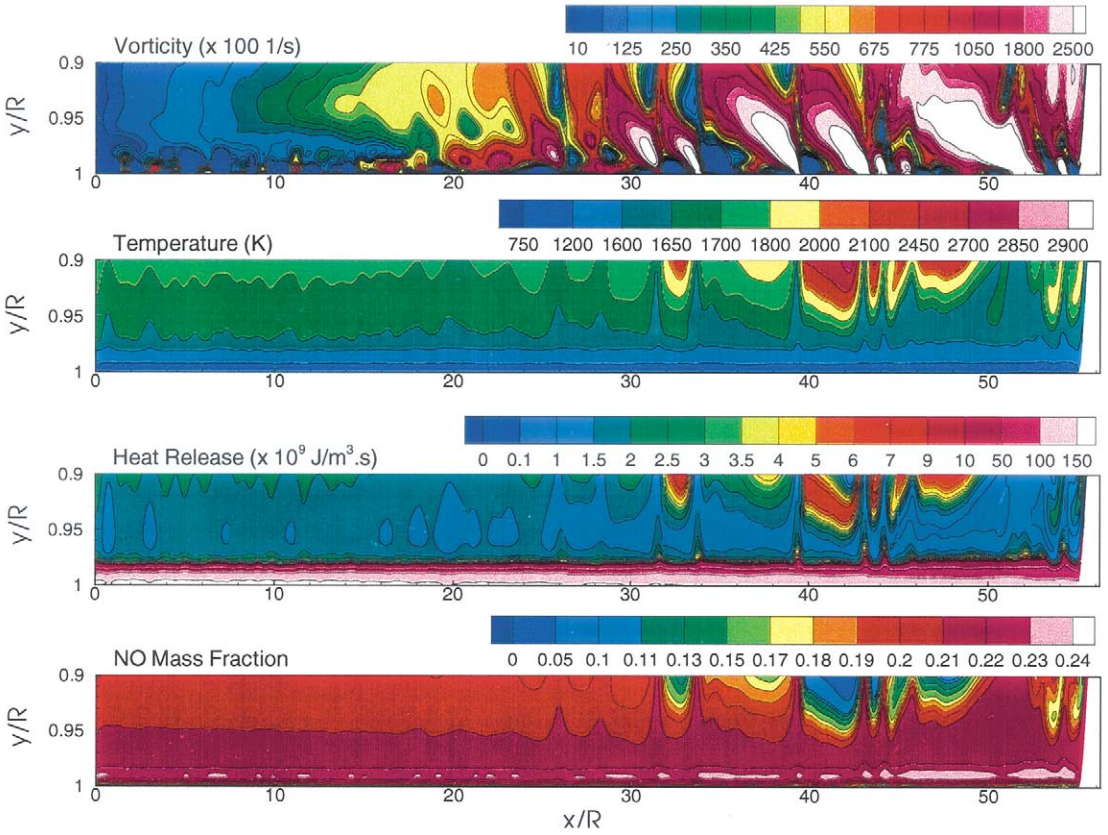
Fig. 7. Close-up view of vorticity, temperature, heat-release, and NO mass-fraction fields immediately above propellant surface, t = 21.7 ms.

$x/R = 45$. The turbulent-eddy and Kolmogorov time scales are approximately 1 ms and 5 μs, respectively. The magnitudes of the Damkohler and Karlovitz numbers vary along the axial direction, however, their radial distributions in the turbulent regime shows that $Da < 1$ and $Ka > 100$ throughout the two-stage flame zone. Both numbers approach their limiting values
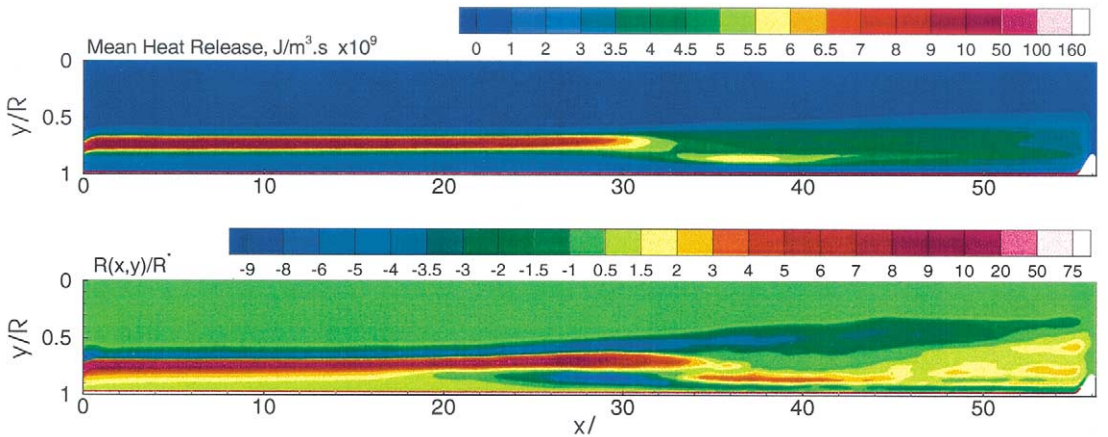
Fig. 14. Distributions of mean heat release and normalized Rayleigh's parameter.
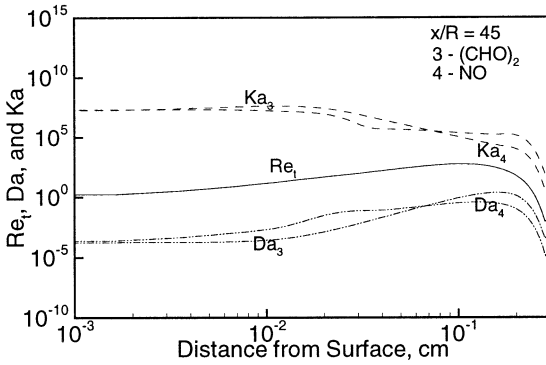
Fig. 8. Distributions of turbulent Reynolds number, Damkohler number, and Karlovitz number within the flame, $x/R = 45$.
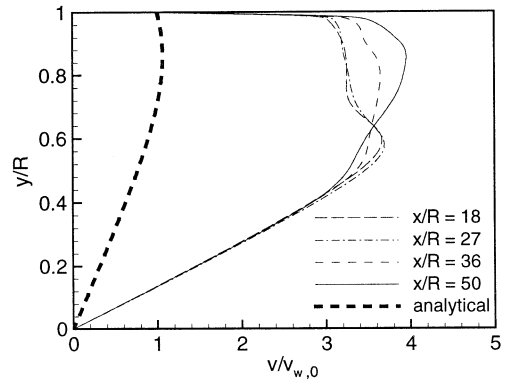

Fig. 10. Radial distributions of radial velocity at various axial locations.

near the end of the secondary flame zone, leading to a highly stretched and thickened flame. The flame extends considerably into the chamber and thus can not be approximated as a thin sheet. It should be noted that the order of magnitude of Ka is much higher than the earlier estimate (shown in Fig. 2) owing to the fact that chemical time scales were used in the present definitions. For high chamber pressures, however, the flame thickness decreases and the well-stirred reactor assumption may become questionable.

Mean Flowfield

The mean flowfield is obtained by performing a time average of the instantaneous quantities over 10 to 12 ms after a stationary flame is obtained, to achieve statistically meaningful data. Figure 9 shows the contour plots of the mean Mach number and pressure. The Mach
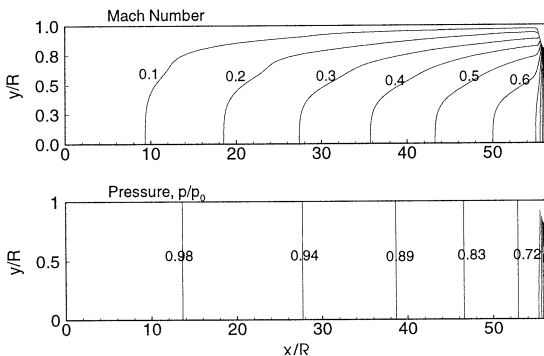

Fig. 9. Contour plots of mean Mach number and pressure.

number increases along the centerline almost linearly from zero at the head end to 0.6 at the nozzle entrance, and the flow becomes supersonic in the divergent section of the nozzle. The flowfield clearly exhibits a two-dimensional structure, with the Mach number near the surface having a much smaller value than that at the centerline. The situation with pressure, however, is substantially different. The pressure decreases from the head end to the nozzle exit as the flow accelerates as a result of the propellant burning. The variations in the radial velocity because of the presence of the flame are small and do not affect the radial pressure distribution. Thus, an almost uniform distribution of the chamber pressure in the radial direction is obtained [19, 20].

Figure 10 shows the radial velocity profiles at different axial locations, normalized with the surface injection velocity at the head end ($v_{w,0}$). The analytical solution obtained by Taylor [4] and Culick [5] for an inviscid, incompressible cold flow is also provided for comparison. It follows a sinusoidal distribution and deviates drastically from that in the present reacting flow case. In the upstream region (e.g., $x/R = 18, 27$), as the gas particle leaves the burning surface, the rapid temperature increase in the primary flame causes the volume to dilate nearly isobarically. Consequently, the fluid element accelerates in the radial direction to maintain mass conservation. The radial velocity further increases in the secondary flame zone and then decreases to zero at the centerline because of flow symmetry. In the highly turbulent region

(e.g., $x/R = 50$), the radial velocity increases rapidly close to the surface and then decreases monotonically towards the centerline. The difference in the flowfield can be attributed to the partial merging of the primary and secondary flames in the turbulent regime, elevating the dark-zone temperatures and thus increasing the peak magnitude of the radial velocity. The distributions of the radial velocity in the primary flame zone are almost identical throughout the chamber. This suggests that despite the strong turbulent flow in the downstream region, turbulence does not penetrate into the primary flame and consequently exerts little influence on the near-surface velocity profile.

The variation of the axial velocity in the radial direction resembles that of a non-reacting injection-driven flow in a porous chamber [13]. The flowfield is basically determined from the balance between the inertial force and the pressure gradient arising from mass injection at the burning surface. The viscous stress is negligible compared with pressure force, except in a narrow region where $x/y \sim O(1/Re)$ near the head-end of the chamber. As the flow undergoes transition to turbulence, the turbulent shear stress causes the axial velocity profiles to gradually steepen near the propellant surface and flatten in the core region. The effect of turbulence on the axial velocity near the burning surface is not significant, further suggesting that turbulence effects near the burning surface are minimal.

Effect of Turbulence on Flame Structure

To study the effect of turbulence-enhanced mixing on the flame structure, variations of the mean temperature and species mass fractions were obtained. They are shown in Figs. 11 and 12, respectively. A two-stage flame structure consisting of the primary-flame, dark, and secondary-flame zones is clearly observed in the upstream laminar region. The flame characteristics such as the thickness of various zones and species and temperature distributions agree well with experimental data as well as the one-dimensional analysis [17]. The overall reaction mechanism for the propellant burning can be globally grouped into the following steps: 1) molecular degradation and ensuing exothermic
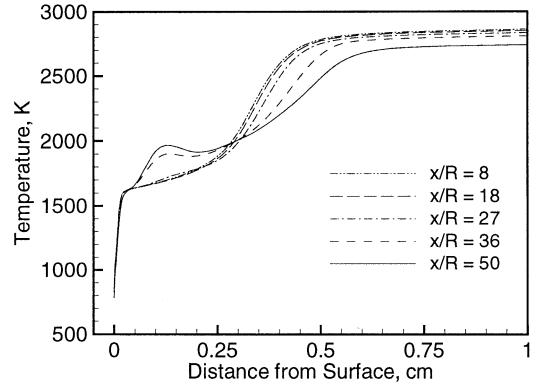

Fig. 11. Radial distributions of temperature at various axial locations.

reactions of NO_2 and aldehydes in the subsurface layer; 2) generation of NO, CO, CO_2, and H_2O, as well as removal of NO_2 and aldehydes, in the primary flame; and 3) reduction of NO to form the final products, such as N_2, CO_2, H_2, and so forth, in the secondary flame [20]. The thickness of the dark zone depends on the chemical-reaction time and the flow-convection time dictated by the radial velocity distribution. In the turbulent region, the enhanced thermal
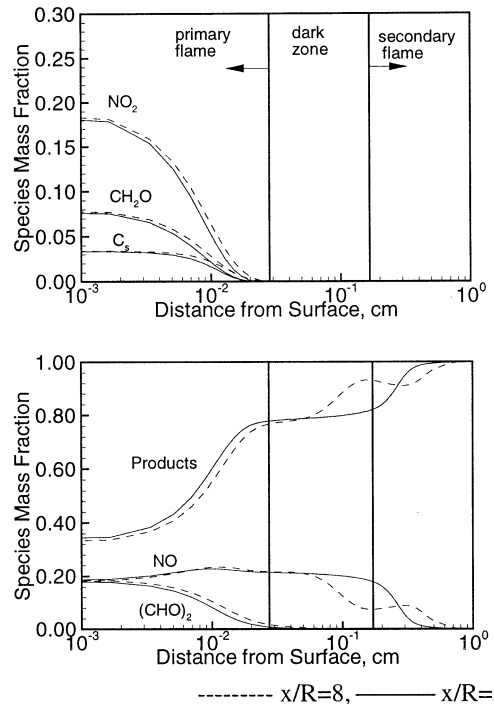

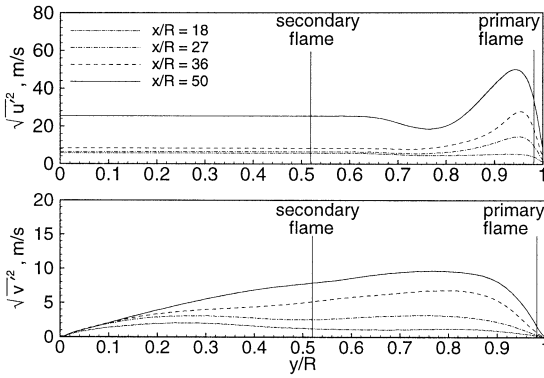Fig. 12. Radial distributions of species mass fractions in laminar and turbulent regimes.

Fig. 13. Axial and radial components of turbulence intensity at various axial locations.

diffusion facilitates NO reduction, which normally occurs at elevated temperatures due to its large activation energy. This process leads to a rapid temperature rise at the end of the primary flame and consequently a thinner dark zone. The temperature plateau around 2000 K may result from the increased radial velocity, which essentially reduces the local flow-residence time required for completing chemical reactions.

Figure 13 shows the radial variations of the axial and radial components of the turbulence intensity at various axial locations. Several points should be noted here. First, the onset of turbulence occurs in regions away from the propellant surface because of the blowing effect created by mass injection from the burning surface [13]. The peak of turbulence intensity tends to move away from the primary flame zone along the chamber. One factor contributing to this phenomenon is the intricate coupling among the flow convection, chemical reaction, and turbulent mixing in the downstream flame zone, as discussed in connection with Figs. 10 and 11. Second, because the flow is dominated by strain rates in the axial direction, the axial turbulence intensity appears to be much greater than its radial counterpart. Third, the chamber pressure of 25 atm at the head end in the present study is lower than the pressure of 65 atm studied in Ref. [19]. The resultant mass burning rate and injection Reynolds number become smaller so that the turbulence intensity near the surface is too weak to exercise any influence on the flame structure. Hence, the mean temperature profile in the primary flame

zone remains unchanged even in the turbulent regime.

Effect of Unsteady Heat Release

The classical approach based on Rayleigh's criterion has demonstrated that under the presence of combustion instabilities, the unsteady fluctuations in heat release are usually in phase with the pressure fluctuations. This enables the fluctuating component of heat release to contribute energy to the amplification of the pressure oscillations, thereby, leading to self-sustained unsteady motions within the motor. Mathematically, the local Rayleigh parameter $R(\mathbf{x})$ is defined as

$$R(\mathbf{x}) = \frac{1}{\tau} \int_{t_0}^{t_0+r} p'(\mathbf{x}, t) q'(\mathbf{x}, t)\ dt \qquad (23)$$

where τ is the time period of oscillation, and $p'(\mathbf{x}, t)$ and $q'(\mathbf{x}, t)$ are the pressure and heat-release fluctuations, respectively. A positive value of $R(\mathbf{x})$ causes local amplification and a negative value leads to damping of oscillatory motions. Integrating Eq. 23 over the entire flow domain gives the global Rayleigh parameter R^*.

Figure 14 shows the distributions of the mean heat-release and normalized Rayleigh parameter $R(\mathbf{x})$, respectively. In the upstream laminar regime, a large amount of heat release occurs in the primary and secondary flame zones. The enhanced heat and mass transfer rates because of turbulent motions in the downstream, however, cause the primary and secondary flames to partially merge and spread the heat release over a thicker region above the propellant surface. The peak value of heat release in the turbulent regime decreases because of reduced flame stiffness. Similarly, the distribution of the Rayleigh parameter indicates drastic differences between the laminar and turbulent regions. The pressure and heat-release fluctuations are positively correlated in the primary flame zone throughout the motor, rendering a positive distribution close to the propellant surface. In the laminar region, the Rayleigh parameter plateaus in the dark zone. The positive and negative peaks in the secondary flame zone suggest a dipole source for driving acoustic instability. In
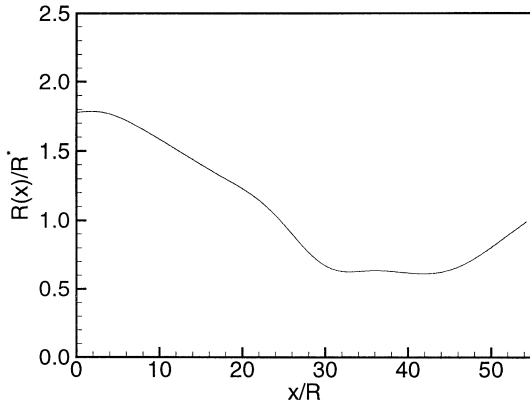
Fig. 15. Axial variation of Rayleigh's parameter.

the transition region (around x/R = 27), one positive and two negative peaks are clearly visible. The positive peak shifts closer to the primary flame in the fully turbulent regime owing to the partial merging of the primary and secondary flames, causing amplification of pressure fluctuations near the burning surface.

Figure 15 shows the axial variation of the Rayleigh parameter $R(x)/R^*$, obtained by integrating $R(x, y)$ in the radial direction. Two important observations are made. First, the magnitude of the spatially averaged Rayleigh parameter is positive throughout the chamber, indicating strong driving mechanisms for unsteady motions within the motor. Second, the magnitude of the Rayleigh parameter decreases from the head end toward the transition region, and becomes almost constant in the fully developed turbulent regime. This may be partially attributed to the existence of an acoustic pressure node in the transition regime. The pressure fluctuation of the first longitudinal mode reaches its minimum in the mid-section of the motor. The enhanced heat and mass transfer because of turbulence further downstream, however, widens the flame and the associated heat-release distribution, compared with the laminar flowfield. The combined effect of pressure and heat-release fluctuations is reflected in the Rayleigh parameter. Accordingly, the Rayleigh parameter decreases from the laminar to the turbulent region. The positive distribution of $R(x)/R^*$ throughout the motor indicates the sustenance of unsteady motions within the chamber.

Analysis of Unsteady Motions

The unsteady flow motions in the chamber can be decomposed into three components: the acoustic, vorticity, and entropy waves. The acoustic wave travels at the speed of sound, while the vorticity and entropy waves are convected downstream at the local fluid velocity. These waves may interact with each other to obtain self-sustained eigenmode oscillations at certain distinct frequencies. Our previous numerical studies on the evolution of injection driven non-reacting flows [13, 14] suggest the existence of several mechanisms of energy transfer between the acoustic/vortical waves and turbulent fluctuations. In the presence of an unsteady flame, entropy waves are generated and modify the above mechanisms. Such interactions are complex and separation of these waves is a formidable task. To explore these mechanisms using the data obtained from numerical simulations, a generalized wave equation in terms of pressure fluctuations is first derived from the conservation equations written in the following vector form [3],

$$\rho \frac{\partial \mathbf{u}}{\partial t} + \rho(\mathbf{u} \cdot \nabla)\mathbf{u} = -\nabla p + F \qquad (24)$$

$$\frac{\partial p}{\partial t} + (\mathbf{u} \cdot \nabla)p = -\gamma p(\nabla \cdot \mathbf{u}) + P \qquad (25)$$

with

$$F = \nabla \cdot \tau_\mu \qquad (26)$$

$$P = \frac{R}{C_\nu}(Q - \nabla \cdot \mathbf{q} + (\tau_\mu \cdot \nabla)\mathbf{u}) \qquad (27)$$

where Q is the rate of heat release because of chemical reactions, $\mathbf{q}$ the heat flux, and τ_μ the viscous stress tensors

$$\tau_{\mu_{ij}} = \mu\left(\frac{\partial u_i}{\partial x_j} + \frac{\partial u_j}{\partial x_i}\right) - \frac{2}{3}\mu\delta_{ij}\nabla \cdot \mathbf{u} \qquad (28)$$

Assuming constant properties, a flow variable $\Im$ is decomposed into the mean $\bar{\Im}$, periodic (i.e., deterministic or organized) fluctuation $\Im^a$, and turbulent motion $\Im^t$,

$$\Im = \bar{\Im} + \Im^a + \Im^t. \qquad (29)$$

The triple decomposition is obtained by defining "long-time" average $\bar{\Im}$ and "short-time" average $\langle\Im\rangle$ as follows

$$\bar{\Im} = \frac{1}{T_\infty} \int_{t_0}^{t_0 + T_\infty} \Im(t + \sigma) \, d\sigma \tag{30}$$

$$\langle \Im \rangle = \frac{1}{T} \int_{t_0}^{t_0 + T} \Im(t + \sigma) \, d\sigma \tag{31}$$

where T is much smaller than T_∞, but much larger than the characteristic time scales of turbulent motions. T_∞ is much larger than the acoustic time scale. The organized and turbulent fluctuations can then be obtained as follows

$$\Im^a = \langle \Im \rangle - \bar{\Im} \tag{32}$$

$$\Im^t = \Im - \bar{\Im} - \Im^a \tag{33}$$

The total time-varying quantity $\Im'$ is the summation of the periodic and turbulent motions

$$\Im' = \Im^a + \Im^t \tag{34}$$

Application of the decomposition defined in Eqs. 29 and 34 to the governing Eqs. 24 and 25, leads to the following wave equation:

$$\nabla^2 p' - \frac{1}{\bar{a}^2} \frac{\partial^2 p'}{\partial t^2} = \Re \tag{35}$$

where $\bar{a} = \sqrt{\gamma R \bar{T}}$ is the speed of sound and $\Re$ the source term involving fluctuations in the velocity, heat-release, entropy, and pressure fields. By taking the short-time average of Eq. 31, the wave equation for organized motions is obtained:

$$\nabla^2 p^a - \frac{1}{\bar{a}^2} \frac{\partial^2 p^a}{\partial t^2} = \langle \Re \rangle. \tag{36}$$

where the source term $\langle \Re \rangle$ can be classified into five major groups of mechanisms affecting pressure oscillations in the chamber.

$$\langle \Re \rangle = I + II + III + IV + V \tag{37}$$

with

$$I = -\nabla \cdot \left(\bar{\rho} \frac{\partial \mathbf{u}^a}{\partial t} \right) + \frac{1}{\bar{a}^2} \frac{\partial}{\partial t} (\bar{\mathbf{u}} \cdot \nabla p^a)$$

$$+ \frac{1}{\bar{a}^2} \frac{\partial}{\partial t} (\mathbf{u}^a \cdot \nabla \bar{p}) + \frac{\gamma}{\bar{a}^2} \frac{\partial}{\partial t} (\bar{p} \nabla \cdot \mathbf{u}^a)$$

$$+ \frac{\gamma}{\bar{a}^2} \frac{\partial}{\partial t} (p^a \nabla \cdot \bar{\mathbf{u}}) \tag{38}$$

$$II = -\nabla \cdot (\bar{\rho} (\bar{\mathbf{u}} \cdot \nabla) \mathbf{u}^a) - \nabla \cdot \left(\frac{p^a}{\bar{a}^2} (\bar{\mathbf{u}} \cdot \nabla) \bar{\mathbf{u}} \right)$$

$$+ \nabla \cdot \left(\frac{\bar{\rho} s^a}{C_p} (\bar{\mathbf{u}} \cdot \nabla) \bar{\mathbf{u}} \right) \tag{39}$$

$$III = -\nabla \cdot (\langle \bar{\rho} (\mathbf{u}' \cdot \nabla \mathbf{u}') \rangle) + \nabla \cdot \left(\frac{\bar{\rho}}{C_p} (\bar{\mathbf{u}} \cdot \nabla) \langle s' \mathbf{u}' \rangle \right) + \nabla \cdot \left(\left\langle \frac{\bar{\rho} s'}{C_p} \mathbf{u}' \cdot \nabla \bar{\mathbf{u}} \right\rangle \right) - \nabla \cdot \left(\left\langle \frac{p'}{\bar{a}^2} (\bar{\mathbf{u}} \cdot \nabla) \mathbf{u}' \right\rangle \right)$$

$$- \nabla \cdot \left(\left\langle \frac{p'}{\bar{a}^2} (\mathbf{u}' \cdot \nabla) \bar{\mathbf{u}} \right\rangle \right) \tag{40}$$

$$IV = -\nabla \cdot \left(\left\langle \frac{p'}{\bar{a}^2} \frac{\partial \mathbf{u}'}{\partial t} \right\rangle \right) + \nabla \cdot \left(\left\langle \frac{\bar{\rho} s'}{C_p} \frac{\partial \mathbf{u}'}{\partial t} \right\rangle \right)$$

$$+ \frac{1}{\bar{a}^2} \frac{\partial}{\partial t} \langle (\mathbf{u}' \cdot \nabla) p' \rangle + \frac{\gamma}{\bar{a}^2} \frac{\partial}{\partial t} \langle (p' \nabla \cdot \mathbf{u}') \rangle \tag{41}$$

$$V = -\frac{1}{\bar{a}^2} \frac{\partial P^a}{\partial t} + \nabla \cdot F^a \tag{42}$$

The entropy fluctuation s' can be determined in terms of pressure and density oscillations as follows:

$$s' = C_p \left(\frac{p'}{\gamma \bar{p}} - \frac{\rho'}{\bar{\rho}} \right) \tag{43}$$

The first group (I) represents temporal development of the correlations between the organized and mean flowfields. The three terms of the second group (II) represent the effect of the mean flowfield on the transport of the periodic motions representing the acoustic, vortical, and entropy waves, respectively. At higher Mach numbers, the mean convective velocity becomes comparable with the acoustic speed and the transport of organized motions by the mean flowfield may become critical. The group (III) represents second-order correlations among the oscillatory velocity, pressure, and entropy fields. These terms are negligible for laminar flows, but become significant for transitional and fully
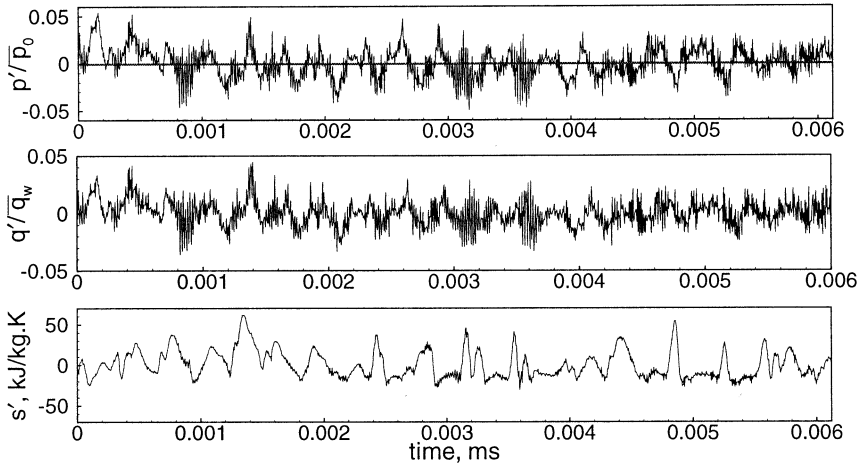
Fig. 16. Time histories of fluctuating pressure, heat-release, and entropy at x/R = 43 and y/R = 0.7.

developed turbulent flows. The group (*IV*) represents temporal evolution of second-order correlations. Finally, the effects of heat release, thermal diffusion, and viscous dissipation on pressure fluctuations are represented by the group (*V*). The above wave equation can be used to perform systematic analysis of the various interaction mechanisms leading to unsteady motions within the chamber.

Figure 16 shows the time histories of fluctuating pressure, heat-release, and entropy in the turbulent secondary flame zone (x/R = 43 and y/R = 0.7). The pressure fluctuation p' is normalized by the mean head-end pressure, while the mean heat release at the propellant surface is used to normalize q'. The magnitude of the pressure oscillation is around 2% of the mean chamber pressure. A broad-band turbulent signal superimposed with peaks corresponding to certain periodic motions is obtained for pressure and heat-release fluctuations. The pressure fluctuations are primarily obtained due to the volume dilatation effects produced by the oscillatory flame (i.e., group *V*). The entropy fluctuation s' obtained from Eq. 43 also indicates strong correlations with p' and q'. Turbulence plays an important role in exciting a range of frequencies corresponding to the hydrodynamic instability, and triggering certain eigenmode oscillations within the chamber (groups *III* and *IV*).

Quantitative information regarding the coupling mechanisms is obtained from the power density spectra of fluctuations in pressure, axial velocity, heat-release, and entropy, as shown in Figs. 17 and 18, respectively. The spectra indicate a range of frequencies being triggered in the laminar (x/R = 8), transitional (x/R = 27), and fully turbulent regions (x/R = 43). In the upstream laminar regime, the axial velocity fluctuation and turbulence intensity level are not significant, but the radial flame oscillation and its ensued heat-release variation lead to self-sustained pressure fluctuations. High-frequency pressure oscillations around 57 kHz (not shown here), corresponding to the first radial mode of the acoustic wave, are also observed because of the rapid flame fluctuations caused by the surface-generated pseudo turbulence. The similarities between the pressure and heat-release spectra suggest strong interactions among them.

The magnitude of axial velocity fluctuation increases in the transitional and fully turbulent regimes with the peak frequency of 3.1 kHz corresponding to the hydrodynamic instability. These vortex-shedding frequencies vary in the axial direction as the local Reynolds number increases. In the downstream turbulent regime, low frequency oscillations (i.e., 850 and 1900 Hz) are triggered and resemble the longitudinal acoustic nodes of the motor. Their magnitudes, however, are much smaller than the hydrodynamic oscillation at 3.1 kHz, possibly because of the effective dissipation of acoustic waves. The first term on the right hand side of Eq. 40 indicates that the correlation $\nabla \cdot (\bar{\rho}\langle \mathbf{u}' \cdot \nabla)\mathbf{u}'\rangle)$ in the fully turbulent regime may sustain large-scale pressure oscillations within the chamber.
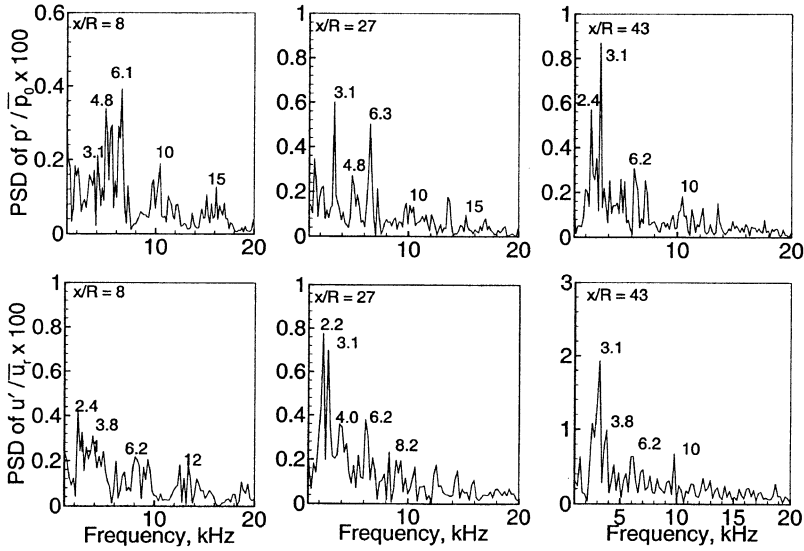
Fig. 17. Power density spectra of pressure and axial-velocity fluctuations at various axial locations, $y/R = 0.7$.

The peaks at 2.2 and 3.1 kHz in the spectra of entropy fluctuations may be attributed to the transport of hot spots across the flame zone by large-scale vortical motions.

Summary of Unsteady Flow Evolution

Figure 19 summarizes the unsteady vorticity, heat-release, entropy, and pressure fields in the combustion chamber. The vorticity fluctuations because of turbulent motion are primarily induced by the oscillatory flame and are convected downstream by the mean flowfield. The magnitude of vorticity fluctuation grows rapidly as the flow undergoes transition to turbulence. Fluctuations in heat-release are related to the variations in convection and chemical time scales. As the velocity field fluctuates, the convection time changes rapidly. The chemical reaction time, on the other hand, is almost unaf-
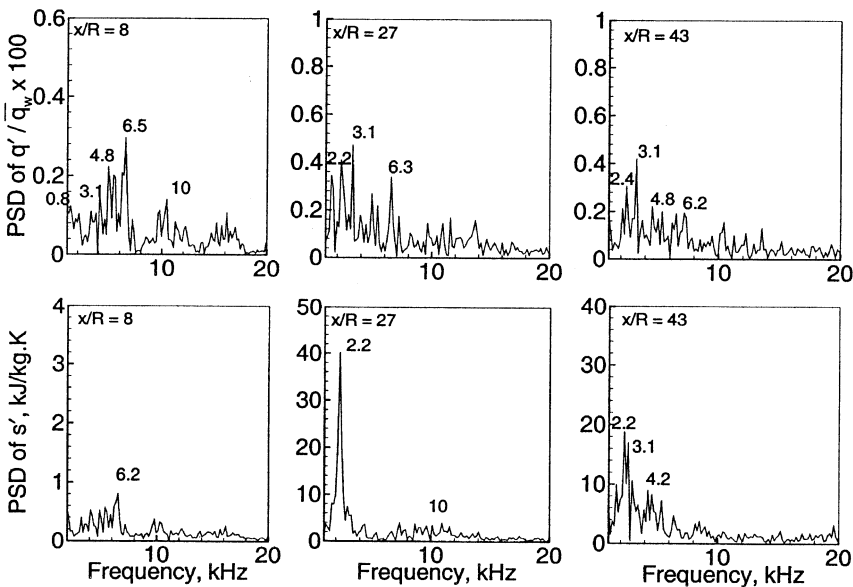

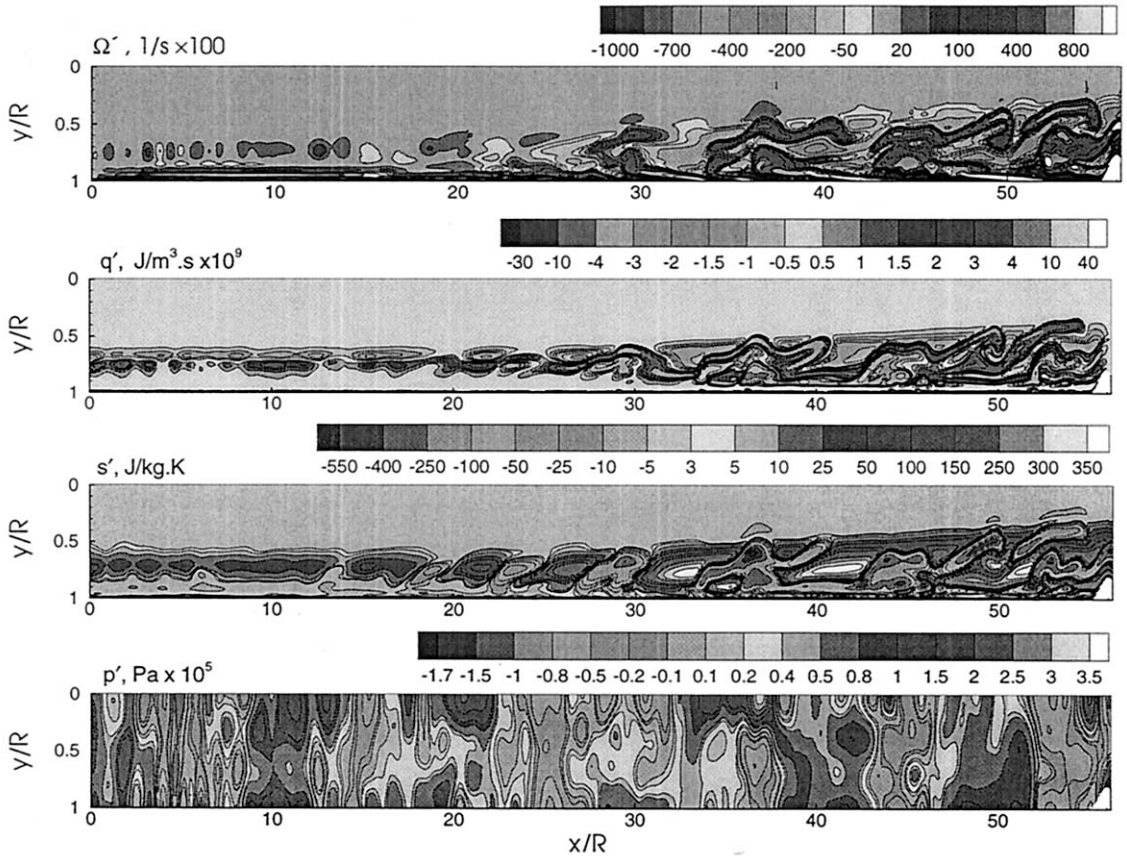Fig. 18. Power density spectra of heat-release and entropy fluctuations at various axial locations, $y/R = 0.7$.

Fig. 19. Snapshots of fluctuating vorticity, heat-release, entropy, and pressure, t = 21.7 ms.

fected in the present case as the combustion of double-base propellants is locally treated as a well-stirred reactor. The heat-release fluctuation, thus, follows the oscillatory vorticity field. The entropy field is derived from its state relationship with pressure and density. Variations in density are closely related with the heat release in the flame zone through the volume dilatation effect. In the present case of distributed reactions, entropy fluctuations occurring at various spatial locations are convected downstream, and then interact with strong gradients in the mean velocity field and excite acoustic oscillations. As in the mean pressure field, the oscillatory pressure is predominantly one-dimensional and exhibits large variations in the axial direction. Turbulence plays an important role in triggering and modifying these waves.

The above phenomena were analyzed in detail by introducing a generalized wave equation in terms of pressure fluctuations. Triple decomposi-

tion of the instantaneous pressure field into the "long-time" average, acoustic, and turbulent fluctuations indicated several source terms involving complex interactions among the acoustic, vortical, and entropy waves as well as turbulent motions. A systematic data deduction based on power-density spectra of pressure, heat-release, velocity, and entropy fluctuations was performed to explore combustion dynamics of homogeneous solid propellants. The present chemical and turbulent models can be utilized to perform parametric studies over a range of chamber pressures to identify the fundamental causes of unsteady motions in a SRM. The data set can be used to calibrate simpler RANS-based turbulence closure schemes.

CONCLUSION

The gas-phase flame dynamics of a double-base homogeneous solid propellant in an axisymmet-

ric rocket motor has been investigated in depth. Turbulence closure was obtained by means of a LES technique that allows a comprehensive analysis of the interactions between propellant combustion and unsteady flow development. A theoretical analysis exploring the coupling between turbulence and flame dynamics is performed to provide insight into self-sustained unsteady motions. The effect of turbulence appears mainly in determining flow structure. The interactions between turbulence and chemical reactions are so weak that the propellant combustion can be locally treated as a well-stirred reactor. Results indicate that the temperature and heat-release distributions in the flame zone exert a significant influence on the flow evolution. The primary flame structure is little affected in the present study because the smooth axial velocity gradient and vertical flow convection prevent turbulence from deeply penetrating into the primary flame. Turbulence-induced large-scale vortical motions, however, may drive flow oscillations with distinct frequencies.

REFERENCES

1. Apte, S. V., and Yang, V., *Proc. Comb. Inst*. 28:903–910 (2000).
2. DeLuca, L., Price, E. W., and Summerfield, M., Eds. *Nonsteady Burning and Combustion Instability of Solid Propellants*, Vol. 143, Progress in Astronautics and Aeronautics, AIAA, Reston, VA, 1992, 873 pages.
3. Culick, F. E. C., and Yang, V., *AIAA Prog. Astro. and Aero*. 143:720–779 (1992).
4. Taylor, G. I., *Proceedings of Royal Society London*, Series 234A, Vol. 11199, 1956, pp. 456–475.
5. Culick, F. E. C., *AIAA J*. 4:1462–1464 (1966).
6. Balakrishnan, G., Linan, A., and Williams, F. A., *J. Propul. Power* 8:1167–1176 (1992).
7. Dunlap, R., Blackner, A. M., Waugh, R. C., Brown, R. S., and Willoughby, P. G., *J. Propul. Power* 6:690–704 (1990).
8. Traineau, J. C., Hervat, P., Kuentzmann, P., AIAA Paper 86-1447, 1986.
9. Beddini, R. A., *AIAA J*. 24:1766–1773 (1986).
10. Sabnis, J. S., Madabhushi, R. K., Gibeling, H. J., and McDonald, H., AIAA Paper 89-2558 (1989).
11. Flandro, G. A., *J. Propul. Power* 11:607–625 (1995).
12. Vuillot, F., *J. Propul. Power* 11:626–639 (1995).
13. Apte, S. V., and Yang, V., *AIAA J*. 39:1577–1586 (2001).
14. Apte, S. V., and Yang, V., *AIAA J*. 40:244–253 (2002).
15. Casalis, G., Avalon, G., Pineau, J-P., *Phy. Fluids* 10:2558–2568 (1998).
16. Ugurtas, B., Avalon, G., Lupoglazoff, N., Vuillot, F., and Casalis, G., *AIAA Prog. Astro. and Aero*. 185:823–836 (2000).
17. Apte, S. V., *Unsteady Flow Evolution and Combustion Dynamics of Homogeneous Solid Propellant in a Rocket Motor*, Ph.D. Thesis, The Pennsylvania State University, December 2000.
18. Flandro, G. A., Cai, W. D., and Yang, V., *AIAA Prog. in Astro. and Aero*. 181:837–858 (2000).
19. Tseng, I. S., and Yang, V., *Combust. Flame* 96:325–342 (1994).
20. Roh, T-S., Tseng, I. S., and Yang, V., *J. Propul. Power* 11:640–665 (1995).
21. Roh, T-S., Apte, S. V., and Yang, V., *Proc. Combust. Inst*. 27:2335–2341 (1998).
22. Roh, T-S., Apte, S. V., and Yang, V., *AIAA Prog. Astro. and Aero*. 181:885–906 (2000).
23. Apte, S. V., and Yang, V., AIAA Paper No. 2000-0709, January 2000.
24. DesJardin, P. E., and Frankel, S. H., *Phys. Fluids* 10:2298–2314 (1998).
25. Erlebacher, G., Hussaini, M. Y., Speziale, C. G., and Zang, T. A., *J. Fluid Mech*. 238:155–185 (1992).
26. Ragab, S. A., and Sheen, S. C., *Large Eddy Simulation of Complex Engineering and Geophysical Flows*. (B. Galperin and S. A. Orszag, Eds.) Cambridge University Press, New York, 1993, pp. 255–285.
27. Peters, N., *AIAA Prog. Astro. and Aero*. 135:155–182 (1991).
28. Peters, N., *Turbulent Combustion*, Cambridge University Press, Cambridge, MA, 2000, pp. 66–86.
29. Poinsot, T., Veynante, D., and Candel, S., *J. Fluid Mech*. 278:1–31 (1994).
30. Hsieh, S. Y., and Yang, V., *Int. J. Comp. Fluid Dyn*. 8:31–49 (1997).